Light-induced frequency shift and relaxation of ground-state 3He via metastability-exchange collisions

Liangyong Wu(吴良勇), Haiyang Yan(闫海洋)

Citation: Chin. Phys. B. 35, 107402 (2026). DOI: 10.1088/1674-1056/aea069 | CSTR: 32038.14.CPB.aea069
http://cpb.iphy.ac.cn; http://iopscience.iop.org/cpb

What follows is a list of articles you may be interested in

Coupled spin Hall effect of ferrite/feromagnetic bilayer films and detection of microwave electromagnetic fields

Dai-Nan Zhang(张岱南), You-Bin Zheng(郑又彬), Xin-Kai Xu(徐鑫锴), Yi-Xin Wang(王益欣), Qing-Hui Yang(杨清慧), Huai-Wu Zhang(张怀武)
Chin. Phys. B. 35, 107504 (2026). DOI: 10.1088/1674-1056/ae24e8 | CSTR: 32038.14.CPB.ae24e8

Pure hyperfine spectra of KRb in its vibronic ground state: Towards the determination of nuclear spin–spin interaction

Qi Ouyang(欧阳琪), Xu-Ping Shao(邵旭萍), Yun-Xia Huang(黄云霞), Xiao-Hua Yang(杨晓华)
Chin. Phys. B. 34, 053302 (2025). DOI: 10.1088/1674-1056/adbdc1 | CSTR: 32038.14.CPB.adbdc1

Suppression of the vapor cell temperature error in a spin-exchange relaxation-free comagnetometer

Jia-Li Liu(刘佳丽), Li-Wei Jiang(姜丽伟), Chi Fang(方驰), Xin Zhao(赵鑫), Yuan-Qiang Chen(陈远强)
Chin. Phys. B. 33, 120701 (2024). DOI: 10.1088/1674-1056/ad84ce

A miniaturized spin-exchange relaxation-free atomic magnetometer based on uniform light field

Jiajie Li(李佳洁), Xiujie Fang(房秀杰), Renjie Li(李任杰), Baodong Chen(陈宝栋), Yueyang Zhai(翟跃阳), Ying Liu(刘颖)
Chin. Phys. B. 32, 053201 (2023). DOI: 10.1088/1674-1056/aca7f2

Tunable coplanar waveguide resonator with nanowires

Zhou Yu(周渝), Jia Tao(郏涛), Zhai Ji-Quan(翟计全), Wang Cheng(汪橙), Zhong Xian-Qian(钟先茜), Cao Zhi-Min(曹志敏), Sun Guo-Zhu(孙国柱), Kang Lin(康琳), Wu Pei-Heng(吴培亨)
Chin. Phys. B. 24, 047403 (2015). DOI: 10.1088/1674-1056/24/4/047403

SPECIAL TOPIC — A 40th Anniversary Celebration: Physics Research and Innovation at Ningbo University

Light-induced frequency shift and relaxation of ground-state ^{3}He via metastability-exchange collisions

Liangyong Wu(吴良勇)[1,2] and Haiyang Yan(闫海洋)[1,†]

[1] *Institute of Fundamental Physics and Quantum Technology, and School of Physical Science and Technology, Ningbo University, Ningbo* 315211, *China*
[2] *Key Laboratory of Nuclear Physics and Ion-beam Application (MOE), Institute of Modern Physics, Fudan University, Shanghai* 200433, *China*

(Received 2 June 2026; revised manuscript received 3 August 2026; accepted manuscript online 31 August 2026)

Metastability-exchange collisions (MECs) play a central role in metastability-exchange optical pumping (MEOP) of ^{3}He, enabling the transfer of polarization from the metastable state to the ground state and the optical detection of nuclear magnetic resonance. Leveraging MECs, optically pumped ^{3}He nuclear magnetometers have been developed since the early development of MEOP. However, the MEC-induced frequency shift can bias the inferred magnetic field and thereby limit accuracy, whereas MEC-induced relaxation shortens the spin-coherence time and reduces the signal-to-noise ratio, thereby limiting sensitivity. Characterizing these two effects is therefore important for improving both the accuracy and sensitivity of ^{3}He magnetometry. In this work, we show that light-induced frequency shifts and relaxation in the metastable state can be transferred to ground-state ^{3}He nuclear spins through MECs. Light shifts are well-known atomic-physics effects and have also been considered in optically detected ^{3}He magnetometry (*Phys. Rev. Research* **7** 043106 (2025)). The focus of the present work is therefore not the identification of the light shift itself, but the quantitative transfer of light-induced frequency shifts and relaxation from metastable atoms to ground-state nuclear spins through MECs. We develop a theoretical model to characterize these light-induced effects, highlight their significance under low-field conditions, and experimentally validate the model.

Keywords: light shift, metastability-exchange collisions, nuclear spin magnetometry

PACS: 74.25.nj, 07.55.Ge, 76.70.Hb

DOI: 10.1088/1674-1056/aea069 **CSTR:** 32038.14.CPB.aea069

1. Introduction

The study of metastability-exchange optical pumping (MEOP) of ^{3}He dates back to the 1960s.[1] Owing to its high efficiency in producing large nuclear polarization, MEOP has become one of the primary techniques for generating hyperpolarized ^{3}He. Hyperpolarized ^{3}He has found broad applications in nuclear physics,[2] magnetic resonance imaging,[3] nuclear spin magnetometry and gyroscopes,[4,5] and tests of fundamental physics.[6–9] These applications benefit from the simple spin-1/2 structure of ^{3}He. In addition, the closed-shell electronic structure of helium effectively shields the nuclear spin from environmental perturbations, giving rise to exceptionally long relaxation and coherence times. At the same time, however, this weak coupling to the environment makes direct optical manipulation and interrogation of ground-state ^{3}He nuclear spins intrinsically challenging.

Noble-gas optical-pumping techniques provide effective routes for overcoming this difficulty. In spin-exchange optical pumping (SEOP),[6] angular momentum is first transferred from light to alkali-metal atoms and then to noble-gas nuclei through spin-exchange collisions. In MEOP, by contrast, light drives optical transitions involving the metastable 2^3S_1 state of ^{3}He, while metastability-exchange collisions (MECs) transfer spin polarization and spin information between the metastable and ground states. Because the population of metastable atoms is generated by a radio-frequency (RF) discharge, the strength of the light–nuclear-spin coupling mediated by MECs can be conveniently controlled by adjusting the discharge intensity. This tunability makes MECs an attractive mechanism not only for producing hyperpolarized ^{3}He, but also for realizing nuclear spin squeezing and quantum memories.[10–12] More recently, MECs have also been exploited to realize optically detected absolute ^{3}He magnetometry.[13]

The ability of MECs to link the optically accessible metastable state with the long-lived ground-state nuclear spin is central to MEC-based detection schemes. MECs are responsible for polarizing ground-state ^{3}He and for transferring nuclear-spin information between the ground and metastable states.[14–17] In the early development of MEOP, this property was used to detect magnetic resonance in the ground state through optical probing of the metastable state.[18–20] Based on this principle, Schearer *et al.*[21] developed an optically detected nuclear magnetometer using MEOP-polarized ^{3}He and measured the Earth's magnetic field with a sensitivity of several microgauss.

While MECs provide the essential bridge between light

†Corresponding author. E-mail: yanhaiyang@nbu.edu.cn

© 2026 Chinese Physical Society and IOP Publishing Ltd. All rights, including for text and data mining, AI training, and similar technologies, are reserved.

and ground-state nuclear spins, they also introduce systematic effects that can limit the performance of ^{3}He magnetometers. In particular, the strong coupling between the ground and metastable states induced by MECs gives rise to frequency shifts and relaxation of the nuclear spins.[22,23] Recently, the MEC-induced frequency shift was carefully measured and corrected by Lu *et al.* in Ref. [13], enabling an absolute ^{3}He magnetometer with a sensitivity of $\sim \mathrm{pT}/\sqrt{\mathrm{Hz}}$. Meanwhile, ME-induced relaxation has been shown to be suppressed in the low-field regime.[24] These developments highlight the need for a quantitative understanding of all MEC-mediated effects that may influence ground-state nuclear spin precession.

Here, we show that MECs can also transfer the light-shift effect from the metastable state to the ground state, leading to additional frequency shifts and relaxation of ground-state ^{3}He nuclear spins. We develop a theoretical model to describe nuclear-spin dynamics under the combined influence of MECs and the light shift, and validate it experimentally. Our results demonstrate that the light shift can have a significant impact in the low-field regime. These findings clarify the role of light-induced effects in spin dynamics under MEOP conditions and provide a framework for characterizing and reducing light-induced systematic errors in ^{3}He magnetometers. For instance, in self-oscillating magnetometers,[21,25–29] where stable pump light is required to sustain polarization, the light-induced frequency shift must be eliminated or controlled to achieve better sensitivity and accuracy.

This paper is organized as follows. In Section 2, we introduce a model describing the light-induced frequency shift and relaxation of ^{3}He nuclear spins. Section 3 presents the experimental setup and measurement principle. In Section 4, we experimentally investigate the light-induced effects under various conditions and compare the results with the model predictions. Finally, Section 5 concludes the paper and discusses future prospects.

2. Model of MEC-mediated light effects

Under discharge conditions, ground-state ^{3}He atoms are strongly coupled to metastable atoms through MECs. It has been shown that the coherence, or transverse nuclear-spin polarization, can be efficiently transferred to the metastable state through MECs, provided that the Larmor frequency in the metastable state is lower than the MEC rate.[15] In addition, MECs modify both the precession frequency and the relaxation rate of ground-state nuclear spins.[18,19,22] In this section, we extend the theoretical description of MECs to include light-induced effects on ground-state spin dynamics.

The evolution of atoms in the ground and metastable states due to MECs can be described as follows:[19]

$$\frac{\mathrm{d}\rho_\mathrm{g}}{\mathrm{d}t} = \frac{1}{T}\left(-\rho_\mathrm{g} + \mathrm{Tr_e}[\rho_\mathrm{m}]\right),$$

$$\frac{\mathrm{d}\rho_\mathrm{m}}{\mathrm{d}t} = \frac{1}{\tau}\left(-\rho_\mathrm{m} + \sum_{F=1/2,3/2} P_F(\mathrm{Tr_n}[\rho_\mathrm{m}]\otimes\rho_\mathrm{g})P_F\right), \quad (1)$$

where ρ_g and ρ_m are the density matrices of the ground and metastable states, respectively. Here, T (~ 1 s) and τ ($\sim 10^{-7}$ s) denote the average time intervals between MECs experienced by atoms in the ground and metastable states, respectively. The large difference between these two time scales arises from the small metastable-state population. As metastable atoms account for only a fraction of $\sim 10^{-6}$ of the total helium population, each metastable atom can undergo MECs with the abundant ground-state atoms. In contrast, a given ground-state atom encounters metastable atoms only rarely, with a probability set by the small ratio n/N, where n and N are the number densities of metastable and ground-state atoms, respectively. As a result, the characteristic MEC time for metastable atoms, τ, is much shorter than that for ground-state atoms, T. The operator P_F projects the metastable-state density matrix onto the two hyperfine subspaces, thereby removing the coherence between them after collisions. The symbols $\mathrm{Tr_n}$ and $\mathrm{Tr_e}$ denote trace operations over the nuclear and electronic degrees of freedom, respectively.

The magnetic field also affects how MECs modify the precession frequency and relaxation time of ground-state ^{3}He. This dependence arises mainly from the mismatch between the gyromagnetic ratios of the ground and metastable states. For a holding field $\boldsymbol{B}_0 = B_0\hat{z}$, the Zeeman Hamiltonian can be written as[19]

$$H_B = -\hbar\left(\frac{4}{3}\gamma_\mathrm{m}\boldsymbol{K}\cdot\boldsymbol{B}_0 + \frac{2}{3}\gamma_\mathrm{m}\boldsymbol{J}\cdot\boldsymbol{B}_0 + \gamma_n\boldsymbol{I}\cdot\boldsymbol{B}_0\right), \quad (2)$$

where $\gamma_\mathrm{m} = -2\pi\times 28.0238144(50)$ kHz/μT[30] and $\gamma_n = -2\pi\times 32.434100033(28)$ Hz/μT[31] denote the gyromagnetic ratios of the ^{4}He metastable state 2^3S_1 and ^{3}He ground state, respectively. The factors $4/3$ and $2/3$ are the Landé g_F factors corresponding to the two hyperfine levels of the metastable state. Here, $\boldsymbol{K}$ and $\boldsymbol{J}$ represent the angular momenta associated with the $F = 1/2$ and $F = 3/2$ hyperfine manifolds of the metastable state, respectively, while $\boldsymbol{I}$ denotes the nuclear spin in the ground state.

Atoms in the metastable state are also affected by the light used for optical pumping or detection, giving rise to the so-called light shift. For optical pumping of the metastable state with circularly polarized light, and under moderate light intensity such that the optical transition rate is slow compared with the decay rate of the excited state, the light shift can be described by the effective Hamiltonian[32,33]

$$H_\mathrm{ls} = -\frac{|E_0|^2}{4}\boldsymbol{\epsilon}^*\cdot\overleftrightarrow{\alpha}\cdot\boldsymbol{\epsilon}, \quad (3)$$

where $\overleftrightarrow{\alpha}$ is the complex polarizability tensor operator of the metastable state, E_0 is the electric-field amplitude of the light, and $\boldsymbol{\epsilon}$ is the complex polarization vector. In general,

$H_{\rm ls}$ is non-Hermitian and can be written as a linear combination of the light-shift operator $\delta\hat{\mathcal{E}} = \frac{1}{2}(H_{\rm ls} + H_{\rm ls}^{\dagger})$, which induces frequency shift, and the light-absorption operator $\delta\hat{\Gamma} = \frac{\rm i}{\hbar}(H_{\rm ls} - H_{\rm ls}^{\dagger})$, which accounts for additional light-induced relaxation in the metastable state. The explicit form of $H_{\rm ls}$ is given in Appendix A.

Taking these effects into account, the evolution of the metastable-state density matrix can be written as

$$\begin{aligned}\frac{{\rm d}\rho_{\rm m}}{{\rm d}t} &= -\frac{\rm i}{\hbar}[H_B + \delta\hat{\mathcal{E}}, \rho_{\rm m}] - \frac{1}{2}\{\delta\hat{\Gamma}, \rho_{\rm m}\} \\ &\quad + \frac{1}{\tau}\left(-\rho_{\rm m} + \sum_{F=1/2,3/2} P_F({\rm Tr_n}[\rho_{\rm m}] \otimes \rho_{\rm g}) P_F\right). \quad (4)\end{aligned}$$

The relaxation associated with the light-absorption operator arises from the depopulation of atoms in the metastable state during optical pumping. The term involving $\delta\hat{\Gamma}$ describes the loss of population from the metastable 2^3S manifold due to optical absorption, which excites atoms to the optically excited 2^3P manifold. Since $\rho_{\rm m}$ is defined only within the metastable manifold, this excitation appears as a depopulation process in the equation of motion for $\rho_{\rm m}$. Taking the trace of $\rho_{\rm m}$ gives ${\rm d}n/{\rm d}t = -\langle\delta\hat{\Gamma}\rangle n$, where $\langle\delta\hat{\Gamma}\rangle$ is the state-averaged optical absorption rate. A complete optical-pumping cycle, however, must also include repopulation, in which atoms return to the metastable state through spontaneous decay from the optically excited states. Following the formalism of Ref. [34], the coupled dynamics of atoms in the ground and metastable states can be described by the following master equations in Lindblad form:

$$\begin{aligned}\frac{\rm d}{{\rm d}t}\rho_{\rm g} &= -{\rm i}[\gamma_{\rm n}\boldsymbol{I}\cdot\boldsymbol{B}_0, \rho_{\rm g}] + \frac{1}{T}(-\rho_{\rm g} + {\rm Tr_e}[\rho_{\rm m}]) - \Gamma_{\rm g}(\rho_{\rm g} - \frac{1}{2}), \\ \frac{\rm d}{{\rm d}t}\rho_{\rm m} &= -\frac{\rm i}{\hbar}\left[\hbar\left(\frac{4}{3}\gamma_{\rm m}\boldsymbol{K} + \frac{2}{3}\gamma_{\rm m}\boldsymbol{J}\right)\cdot\boldsymbol{B}_0 + \delta\hat{\mathcal{E}}, \rho_{\rm m}\right] \\ &\quad + \sum_{q,F}\gamma_{\rm r}\left(L_{q,F}\rho_{\rm m}L_{q,F}^{\dagger} - \frac{1}{2}\{L_{q,F}^{\dagger}L_{q,F}, \rho_{\rm m}\}\right) \\ &\quad + \frac{1}{\tau}\left(-\rho_{\rm m} + \sum_F P_F\{{\rm Tr_n}[\rho_{\rm m}]\otimes\rho_{\rm g}\}P_F\right) \\ &\quad - \gamma_{\rm r}^S\left(\rho_{\rm m} - \frac{1}{6}\right), \quad (5)\end{aligned}$$

where $\gamma_{\rm r}$ is the spontaneous decay rate and $L_{q,F}$ are the Lindblad operators. By comparing the second equation in Eq. (5) with Eq. (4), the light-absorption operator can be identified as $\delta\hat{\Gamma} = \sum_{q,F}\gamma_{\rm r}L_{q,F}^{\dagger}L_{q,F}$, which represents the removal of atoms from the corresponding metastable sublevels. In contrast, the term $\gamma_{\rm r}L_{q,F}\rho_{\rm m}L_{q,F}^{\dagger}$ describes the repopulation of these sublevels through spontaneous decay from the optically excited states. The last terms in Eq. (5) account for additional relaxation processes in the ground and metastable states caused by collisions and discharge-induced quenching, with $\Gamma_{\rm g}$ and $\gamma_{\rm r}^S$ denoting the corresponding relaxation rates. The explicit form of $L_{q,F}$ for metastable ^{3}He is derived in Appendix B.

To gain physical insight into how MECs modify the frequency shift and relaxation of ground-state ^{3}He, we first examine the dynamics of the expectation values of the angular momenta $\langle\boldsymbol{K}\rangle$, $\langle\boldsymbol{J}\rangle$, and $\langle\boldsymbol{I}\rangle$. In the absence of the light shift, the evolution equations for their transverse components are

$$\begin{aligned}\frac{\rm d}{{\rm d}t}\langle I_+\rangle &= \left[-{\rm i}\gamma_{\rm n}B_0 - \left(\frac{1}{T} + \Gamma_{\rm g}\right)\right]\langle I_+\rangle + \frac{1}{3T}(\langle J_+\rangle - \langle K_+\rangle), \\ \frac{\rm d}{{\rm d}t}\langle K_+\rangle &= \left(-{\rm i}\frac{4}{3}\gamma_{\rm m}B_0 - \frac{7}{9\tau}\right)\langle K_+\rangle + \frac{1}{9\tau}\langle J_+\rangle - \frac{1}{9\tau}\langle I_+\rangle, \\ \frac{\rm d}{{\rm d}t}\langle J_+\rangle &= \left(-{\rm i}\frac{2}{3}\gamma_{\rm m}B_0 - \frac{4}{9\tau}\right)\langle J_+\rangle + \frac{10}{9\tau}\langle K_+\rangle + \frac{10}{9\tau}\langle I_+\rangle. \quad (6)\end{aligned}$$

Here, $I_+ = I_x + {\rm i}I_y$, $K_+ = K_x + {\rm i}K_y$, and $J_+ = J_x + {\rm i}J_y$ denote the transverse components of the corresponding angular momenta. Since $\tau \ll T$, the metastable-state variables $\langle K_+\rangle$ and $\langle J_+\rangle$ evolve on a much faster timescale than the ground-state variable $\langle I_+\rangle$. On the timescale of the ground-state evolution, they can therefore be solved in terms of $\langle I_+\rangle$, yielding an effective relation between $\langle J_+\rangle - \langle K_+\rangle$ and $\langle I_+\rangle$. Substituting this relation into the first equation gives the effective evolution equation for $\langle I_+\rangle$.

The resulting equation can be written as[18]

$$\frac{\rm d}{{\rm d}t}\langle I_+\rangle = \left[-{\rm i}\left(\gamma_{\rm n}B_0 - \frac{{\rm Im}[\beta]}{T}\right) - \left(\frac{1-{\rm Re}[\beta]}{T} + \Gamma_{\rm g}\right)\right]\langle I_+\rangle, \quad (7)$$

where

$$\beta = \frac{1}{3}\frac{7{\rm i}\gamma_{\rm m}B_0\tau + 3}{(1+{\rm i}\gamma_{\rm m}B_0\tau)(1+4{\rm i}\gamma_{\rm m}B_0\tau)}. \quad (8)$$

The real and imaginary parts of β are given by

$${\rm Re}[\beta] = \frac{3 + 23(\gamma_{\rm m}B_0\tau)^2}{3\left[1 + 17(\gamma_{\rm m}B_0\tau)^2 + 16(\gamma_{\rm m}B_0\tau)^4\right]}, \quad (9)$$

$${\rm Im}[\beta] = -\frac{8\gamma_{\rm m}B_0\tau + 28(\gamma_{\rm m}B_0\tau)^3}{3\left[1 + 17(\gamma_{\rm m}B_0\tau)^2 + 16(\gamma_{\rm m}B_0\tau)^4\right]}. \quad (10)$$

Accordingly, the MEC-induced frequency shift and relaxation rate are

$$\Delta\omega_{\rm ME} = -\frac{{\rm Im}[\beta]}{T} = \frac{8\gamma_{\rm m}B_0\tau + 28(\gamma_{\rm m}B_0\tau)^3}{3T\left[1 + 17(\gamma_{\rm m}B_0\tau)^2 + 16(\gamma_{\rm m}B_0\tau)^4\right]}, \quad (11)$$

$$\Gamma_{\rm ME} = \frac{1-{\rm Re}[\beta]}{T} = \frac{28(\gamma_{\rm m}B_0\tau)^2 + 48(\gamma_{\rm m}B_0\tau)^4}{3T\left[1 + 17(\gamma_{\rm m}B_0\tau)^2 + 16(\gamma_{\rm m}B_0\tau)^4\right]}. \quad (12)$$

These expressions show that MECs modify both the precession frequency and the relaxation rate of the ground-state nuclear spin. In the low-field limit, the MEC-induced frequency shift scales linearly with $\gamma_{\rm m}B_0\tau$, whereas the MEC-induced relaxation rate is a second-order effect, scaling as $(\gamma_{\rm m}B_0\tau)^2$.

At high fields, the frequency shift decreases approximately as $1/(\gamma_m B_0 \tau)$, while the relaxation rate approaches $1/T$. Therefore, the MEC-induced frequency shift reaches a maximum at an intermediate magnetic field, whereas the MEC-induced relaxation increases from zero and gradually saturates in the high-field limit. Physically, these effects arise because MECs repeatedly couple the long-lived ground-state nuclear spin to the metastable-state spin dynamics, whose precession frequencies and relaxation rates differ from those of the ground state. The influence of the metastable state is encoded in the complex parameter β: its imaginary part produces a shift of the precession frequency, while its real part determines the correction to the relaxation rate.

When the light shift is included, the vector component of the light-shift operator $\delta\hat{\mathcal{E}}$ (see Appendix A) acts as an effective magnetic field on atoms in the metastable state. This component takes the form $\delta\hat{\mathcal{E}} \propto \boldsymbol{S}\cdot(2\boldsymbol{K}+\boldsymbol{J})$, where $\boldsymbol{S}$ denotes the photon spin. As a result, the metastable-state angular momentum precesses in the combined field of the holding field and the light-induced effective field. This modifies the MEC-mediated coupling between the metastable and ground states, thereby changing the MEC-induced frequency shift and the relaxation of the ground-state nuclear spin. In addition, the light-absorption operator $\delta\hat{\Gamma}$ introduces extra relaxation in the metastable state, which can be transferred to the ground-state nuclear spin through MECs.

For clarity, the effective fields associated with the vector light shift in the two metastable hyperfine manifolds can be estimated from (see Appendix A)

$$B_{\mathrm{ls}}^{(1/2)} = \frac{3 f_{8,9} I e^2}{8\hbar\gamma_m c\varepsilon_0 m_e}\,\mathrm{Re}\left[\frac{Z(\omega;\omega_{8,9})}{\omega_{8,9}}\right] s_z, \tag{13}$$

where $f_8 = 0.078963$ ($f_9 = 0.0503611$) is the oscillator strength of C_8 (C_9) transition, I is the light intensity, $Z(\omega;\omega_{8,9})$ is the Doppler-averaged complex line-shape function defined in Appendix A, and s_z is the photon helicity. Substitution of $I \simeq 100\ \mathrm{mW/cm^2}$, the Doppler width $D \simeq 2\pi \times 1.19$ GHz, and the gyromagnetic ratio given above yields a maximum dispersive field of order several microtesla. This is an effective field acting directly on the metastable-state atoms, not a magnetic field directly experienced by the ground-state nuclei. Its influence on the latter is reduced and transferred through MECs, as described by the correction $-\mathrm{Im}[\beta]/T$ in Eq. (7). The influence of the pump light is therefore expected to become particularly important in the low-field regime.

To quantitatively describe these light-induced effects, we solve Eq. (5) numerically using the separation between the fast metastable-state dynamics and the slow ground-state evolution. Because ρ_g evolves on the macroscopic timescale T, it varies only weakly over the much shorter timescale of the metastable-state dynamics. We therefore treat ρ_g as fixed when solving for ρ_m. At each time step, ρ_m is first obtained from its steady-state equation for the current value of ρ_g, and the resulting ρ_m is then used to update ρ_g through the ground-state evolution equation.

3. Experimental setup and measurement method

The measurements were performed using a low-field ^{3}He MEOP apparatus with MEC-assisted optical detection, as shown in Fig. 1. A small fraction of ^{3}He atoms is excited into the metastable state by a RF discharge operated at 1.17 MHz with a power of about 0.9 W. The metastable atoms are then polarized by a circularly polarized pump laser resonant with the C_8 transition.[35] The pump beam is expanded to cover the entire cell volume, and an optical shutter (OS) is used to switch the optical pumping on and off. Through MECs, as illustrated in Fig. 1(b), the polarization of metastable atoms is transferred to the ground-state nuclei, thereby producing nuclear spin polarization.

To suppress magnetic noise and provide a highly uniform holding field, the cell is placed inside a five-layer μ-metal magnetic shield, which reduces the ambient magnetic field to the 10-nT level. The holding field is generated by a Merritt coil system. After optical pumping, a resonant RF pulse generated by a Helmholtz coil surrounding the cell tips the nuclear spin polarization into the transverse plane. The nuclear spins then undergo free precession in the holding field, and the precession amplitude decays due to relaxation processes, producing a free induction decay (FID) signal. For the pump-off measurements, the OS is closed before the RF pulse and remains closed throughout the FID acquisition. For the pump-on measurements, the pump beam remains on during both the RF pulse and the FID acquisition. At each holding field and for each optical condition, the RF-pulse duration is scanned at fixed RF amplitude, and the $\pi/2$ condition is identified by maximizing the initial transverse FID amplitude.

The FID signal is detected optically using a weak ($\sim$ 1 mW) linearly polarized probe beam propagating along the x axis. The probe detuning is $\Delta_p = -1$ GHz relative to the C_9 transition. Here, the light-shift effects induced by the probe beam are not considered. Since the probe beam is linearly polarized, its vector light shift is negligible because the mean photon spin vanishes for ideal linear polarization ($s = 0$). Possible residual circular polarization due to experimental imperfections only induces a second-order frequency shift, as the corresponding effective magnetic field is transverse to the holding field B_0, which is much smaller than the pump-light-induced shift. The projection of the metastable-state angular momenta $\boldsymbol{K}$ and $\boldsymbol{J}$ along the probe-beam propagation direction directly produces the Faraday rotation. Owing to rapid

MECs, the metastable-state angular momenta follow the dynamics of the ground-state nuclear spins; the latter can therefore be read out indirectly by monitoring this metastable-state Faraday rotation. This polarization rotation is measured with a homodyne detection scheme. To improve the signal-to-noise ratio, the probe signal is modulated by a photoelastic modulator (PEM) and subsequently demodulated with a lock-in amplifier.

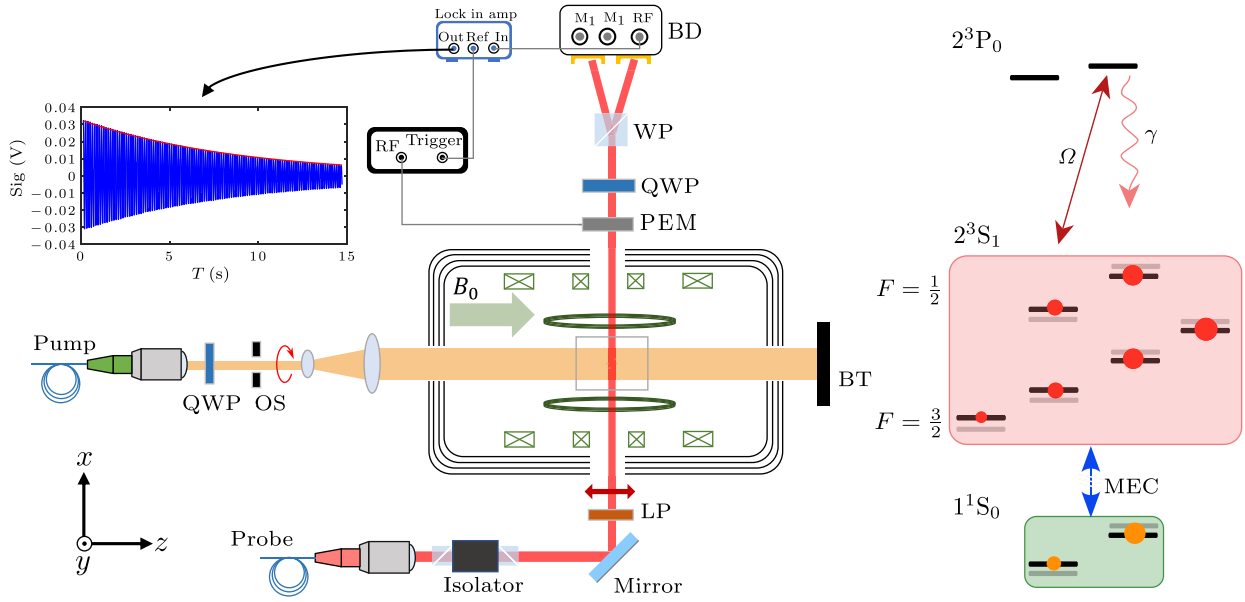

Fig. 1. (a) Experimental setup of the MEC-based ^{3}He polarization and detection system. The apparatus consists of three main parts: a magnetic-field system based on Merritt coils enclosed in a five-layer μ-metal magnetic shield; an optical-pumping system including a $\sim$ 1 W pump laser, polarization-control optics, and beam-expansion optics; and a signal-detection system using a weak ($\sim$ 1 mW) linearly polarized probe laser propagating transverse to the pump beam, together with a homodyne detection scheme. The PEM supplies a time-dependent retardance at approximately 50 kHz, while the QWP supplies the static retardance used to set the operating point of the polarization-modulation detection; the Faraday-rotation signal is then analyzed by the Wollaston prism and balanced detector and demodulated by the lock-in amplifier. The inset shows a typical FID signal demodulated by a lock-in amplifier. LP: linear polarizer; QWP: quarter-wave plate; OS: optical shutter; BT: beam trap; BD: balanced detector; PEM: photoelastic modulator; WP: Wollaston prism. (b) Relevant hyperfine energy levels of ^{3}He involved in MEOP. The metastable and ground states are coupled through MECs. The red double arrow indicates the optical-pumping transition, and the wavy line represents spontaneous decay from the excited state. The light shift modifies the Zeeman sublevels of the metastable state and, through MECs, also affects the ground-state nuclear spin.

The Larmor frequency and relaxation rates of the ^{3}He nuclear spin are extracted by fitting the FID signal to

$$S_x(t) = S_0 \sin(2\pi f_0 t + \phi)\, \mathrm{e}^{-t/T_2} + S_1\, \mathrm{e}^{-t/T_1}, \qquad (14)$$

where $f_0 = \gamma_n B/(2\pi)$ is the Larmor frequency, T_2 and T_1 are the transverse and longitudinal relaxation times, respectively, and ϕ is the initial phase. The first term in Eq. (14) describes the decaying transverse spin coherence that gives rise to the oscillatory FID signal. The second term is included phenomenologically to account for a slowly varying non-oscillatory background in the detected signal.

This non-oscillatory contribution can arise from a small misalignment between the pump and probe beams. Ideally, the pump and probe beams are orthogonal, so that the probe detects only the transverse spin component after the RF pulse. In practice, a small misalignment can project part of the longitudinal polarization prepared by optical pumping onto the probe direction. This projected component does not contribute to the Larmor precession and therefore appears as a slowly varying background in $S_x(t)$. If the pump light is switched off during FID detection, this contribution decays through longitudinal relaxation and is proportional to e^{-t/T_1}. If the pump light remains on, the corresponding background is governed by the balance between optical pumping and relaxation and may approach a steady-state value. In our measurements, this slowly varying contribution is included phenomenologically by the second term in Eq. (14).

4. Experimental characterization of light-induced effects

In this section, we characterize the light-induced frequency shift and relaxation under different experimental conditions, including different RF discharge strengths, magnetic-field strengths, laser detunings, and pump-laser powers. The measured dependences are compared with the theoretical model developed in Section 2. Note that each data point in Figs. 2–4 represents the mean value of three repeated measurements. The standard deviations of these measurements are smaller than the marker size and are therefore not visible in the figures.

As indicated by Eq. (7), the MEC-induced frequency shift in the low-field limit is approximately $\Delta\omega_{\mathrm{ME}} \simeq 8\gamma_m B_0 \tau/(3T)$.

Since τ is mainly determined by the ground-state number density, whereas T is inversely proportional to the metastable-state density, the frequency shift is expected to scale with the metastable-state population, which is controlled by the RF discharge. The metastable-state density is not, in general, required to be linear in the RF-generator amplitude.

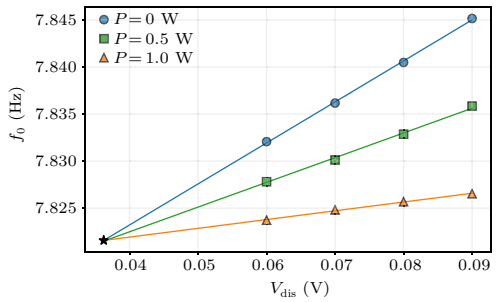

Fig. 2. Larmor frequency as a function of the RF-generator amplitude V_{dis} for different pump-laser powers. The blue circles, green squares, and yellow triangles represent experimental data obtained at different pump-laser powers, and the solid lines are linear fits. The black star indicates the extrapolated crossing point of the fitted lines.

Figure 2 shows the measured Larmor frequency as a function of discharge strength. Here, V_{dis} denotes the amplitude of the RF signal generator, which controls the RF discharge strength in the ^{3}He cell. The blue circles show the precession frequencies measured with the pump beam blocked. In this case, the Larmor frequency varies linearly with V_{dis}, consistent with the fact that a stronger discharge produces a larger metastable-state population and therefore a larger MEC-induced frequency shift. Over the measured interval, approximately $0.06\ \text{V} \leq V_{dis} \leq 0.09\ \text{V}$, the Larmor frequency is empirically well described by a linear function of V_{dis}. We use this local linear fit only as a parametrization of the data; it is consistent with an approximately linear increase in the effective metastable-state density over this restricted range, but it is not intended to establish a general linear relation between discharge amplitude (or power) and metastable-state density.

When the pump beam is on, the measured frequencies also show an approximately linear dependence on V_{dis} within the same restricted interval, as shown by the yellow triangles and green squares. However, their slopes differ from that obtained with the pump beam blocked. This difference indicates that the pump light introduces an additional frequency shift. The mechanism discussed in Section 2 explains this behavior: the light shift acts on the metastable state and is transferred to the ground-state nuclear spin through MECs. Its effect, therefore, depends on the metastable-state population and becomes stronger at larger discharge strengths. A weaker discharge is therefore preferable for reducing this light-induced systematic frequency shift in high-accuracy ^{3}He magnetometry.

The local linear fits extrapolate to a common point at $V_{dis} \approx 0.035$ V, which coincides with the independently observed extinction threshold of the RF discharge. We do not assume that a measurement performed with a finite metastable-state population is free of MEC-induced shifts. Rather, we interpret the crossing point as the extrapolated limit $n_m \to 0$. Because $1/T \propto n_m$, both the ordinary MEC-induced correction and the MEC-mediated pump-light correction vanish in this limit. The frequency $\omega_g = 2\pi \times 7.821$ Hz is therefore used as an estimate of the unperturbed ground-state Larmor frequency. Since no optical FID signal can be obtained after the discharge is extinguished, this value is necessarily an extrapolation rather than a direct measurement at zero discharge.

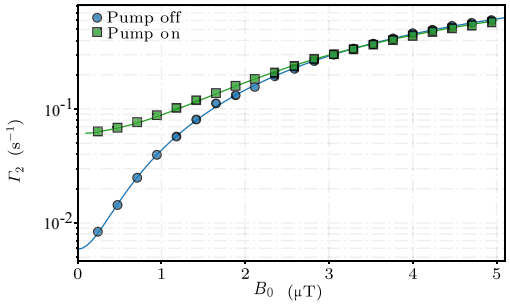

Fig. 3. The transverse relaxation rate Γ_2 as a function of the magnetic-field strength under pump-on and pump-off conditions. The green squares and blue circles represent the experimental results. The blue line denotes the fit to the data using Eq. (15), while the green line represents the numerical results calculated using the parameters obtained from the fit.

The influence of MECs and pump light on nuclear spin precession depends strongly on the holding field B_0. Figure 3 shows the transverse relaxation rate Γ_2 measured at different magnetic-field strengths. The blue circles and green squares represent the relaxation rates extracted from the FID signals under pump-off and pump-on conditions, respectively.

When the pump beam is off, the transverse relaxation rate is described by the analytic expression[18]

$$\Gamma_2 = \Gamma_g + \frac{1}{T}\left[1 - \frac{4}{9}\frac{1}{1+(\gamma_m B_0 \tau)^2} - \frac{5}{9}\frac{1}{1+(4\gamma_m B_0 \tau)^2}\right]. \quad (15)$$

Fitting the pump-off data with Eq. (15) yields the blue curve in Fig. 3. From this fit, we obtain a ground-state relaxation rate of $\Gamma_g = (5.96 \pm 2.94) \times 10^{-3}\ \text{s}^{-1}$, together with average MEC times of $T = 0.37 \pm 0.02$ s for the ground state and $\tau = (2.23 \pm 0.08) \times 10^{-7}$ s for the metastable state, where the uncertainties are one-standard-error values from the fit covariance matrix. The extracted value of τ is consistent with that reported in Ref. [36]. These parameters are then used as fixed inputs in the numerical solution of Eq. (5). The green curve in Fig. 4 is obtained from the numerical calculation using the parameters listed in Table 1. The measured pump-on relaxation rates agree well with the theoretical prediction, indicating that the observed increase in Γ_2 can be explained by light-induced relaxation in the metastable state that is transferred to the ground-state nuclear spin through MECs.

As predicted by Eq. (15), the blue curve approaches the high-field limit of $\Gamma_g + 1/T$. In the low-field regime, where

$B_0 \ll 1/|\gamma_m \tau| \approx 25$ μT, the MEC-induced relaxation is suppressed, and the relaxation time approaches $1/\Gamma_g$ as the magnetic field approaches zero. This behavior is reminiscent of the spin-exchange-relaxation-free regime observed in alkali-metal magnetometers,[38] although the underlying mechanism is different.

When the pump light is applied, as shown by the green curve, the nuclear relaxation is significantly enhanced, especially at low magnetic fields. In the near-zero-field regime, the relaxation time is reduced to approximately 15 s. As the magnetic field increases, the influence of the pump light becomes less pronounced. This result highlights the need to account for light-induced relaxation when using MEOP-polarized ^{3}He in low-field precision measurements.

Finally, we examine how the light-induced frequency shift and relaxation depend on the pump-light detuning and intensity, as shown in Fig. 4. The blue squares and green circles represent the measured frequency shifts and relaxation rates, respectively, and the lines show the numerical results obtained from Eq. (5). Overall, the measurements agree well with the numerical predictions. The remaining discrepancies may arise from uncertainties in the input parameters used in the simulations, such as the laser power, as well as from the simplified assumption of a uniform laser-intensity profile across the cell. In addition, since $\Delta\omega_{ME} \propto 1/T$, the relative uncertainty in T produces approximately the same relative uncertainty in the MEC-induced shift. The characteristic field scale is set by $|\gamma_m \tau|^{-1}$, so uncertainty in τ mainly shifts the field dependence horizontally. In the weak-to-moderate intensity regime, the vector light shift is approximately proportional to the laser power I, and the relative intensity-calibration uncertainty therefore propagates approximately linearly to the predicted light-induced shift. The optical parameters D, γ_r, and γ_r^S mainly affect the magnitude and width of the calculated response near resonance and are plausible sources of the residual discrepancy. By contrast, the relative uncertainties of γ_m and γ_n are many orders of magnitude smaller than the experimental uncertainties and have a negligible effect on the calculated curves.

Figure 4(a) shows the dependence on laser detuning. The light-induced relaxation is largest near resonance with the C_8 transition and decreases as the laser is detuned from resonance. This behavior is expected because the laser-induced broadening of the metastable-state magnetic-resonance linewidth is strongest on resonance.[39] Through MECs, this enhanced relaxation in the metastable state is transferred to the ground-state nuclear spin. As a result, the ground-state relaxation time is significantly shortened near resonance and approaches the value measured without pump light when the detuning exceeds 3 GHz.

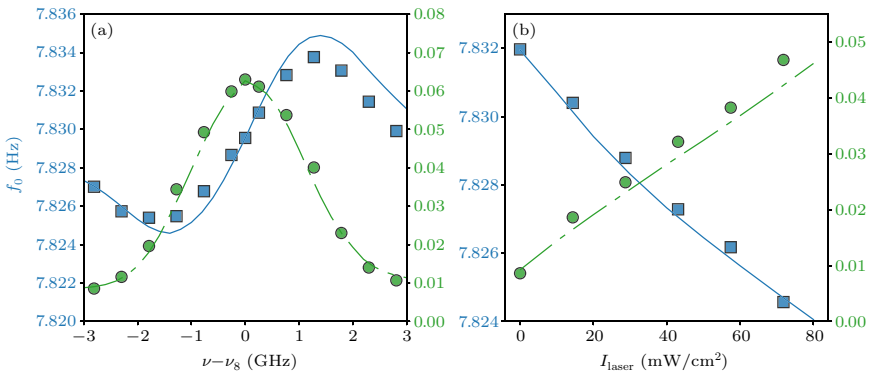

Fig. 4. Dependence of the pump-light-induced frequency shift and relaxation on laser detuning and intensity. The blue squares represent the measured frequency shifts, plotted on the left vertical axis, while the green circles represent the measured relaxation rates, plotted on the right vertical axis. The lines show the corresponding numerical results. In the left panel, the laser detuning is defined relative to the C_8 transition, with the pump-light intensity fixed at approximately 66 mW/cm^2. In the right panel, the pump laser is red-detuned by approximately 1 GHz from the C_8 transition.

Table 1. Parameters used in the numerical solution of Eq. (5) and for plotting the curves in Figs. 3 and 4. The parameters γ_r, γ_r^S, and D are used to calculate the transition rates associated with the jump operators L_μ (see Appendix B). The source and treatment of the uncertainties for each parameter are now listed explicitly.

Parameter	Value	Source	Uncertainty/treatment
T	0.37 s	Fit to Fig. 3	0.02 s (fit)
τ	2.2×10^{-7} s	Fit to Fig. 3	0.08×10^{-7} s (fit)
Γ_g	5.9×10^{-3} s^{-1}	Fit to Fig. 3	2.94×10^{-3} s^{-1} (fit)
I	66 mW/cm^2	Measured at the cell	1% calibration
γ_r^S	1.022 kHz	Ref. [37]	Fixed literature value
γ_r	10.22 MHz	Ref. [37]	Fixed literature value
D	1.18 GHz	Ref. [37]	Fixed literature value
γ_m	$-2\pi \times 28.0238144(50)$ kHz/μT	Ref. [37]	Quoted in parentheses
γ_n	$-2\pi \times 32.434100033(28)$ Hz/μT	Ref. [37]	Quoted in parentheses

The light-induced frequency shift exhibits a dispersive dependence on laser detuning, as also shown in Fig. 4(a). As the laser frequency is scanned across the C_8 resonance, a relative Larmor-frequency shift of nearly 10 mHz is observed. The finite frequency shift observed at zero detuning is defined relative to the Larmor frequency of 7.832 Hz measured without pump light. This residual shift is attributed to the nearby C_9 transition, which is also weakly addressed by the pump light.

Figure 4(b) shows the dependence of the light-induced frequency shift and relaxation on pump-laser power, with the laser wavelength red-detuned by approximately 1 GHz from the C_8 transition. The observed power dependence is also well reproduced by the numerical model. Since MECs induce a positive frequency shift,[18,19] whereas the light-induced shift depends on both laser detuning and intensity, the pump-light parameters provide an additional degree of freedom for controlling the net frequency shift. For applications involving modulated or differential magnetic-field measurements, stable frequency offsets can in principle be rejected by the measurement protocol. In absolute magnetometry, however, such offsets directly affect the inferred magnetic field and must be characterized or compensated. The tunability of the light-induced shift therefore provides a useful tool for reducing systematic frequency shifts in MEC-assisted optically detected absolute ^{3}He magnetometers.[13,22]

Beyond the light-induced shift, various effects such as laser heating, RF discharge fluctuations, and magnetic-field drift may also contribute to the frequency shift. Therefore, we analyzed the potential shifts caused by these systematic effects. Laser heating is expected to be small because of the low absorption of the glass cell near 1083 nm, combined with the weak absorption from the low density of metastable ^{3}He atoms. By comparison, in similar SEOP ^{3}He cells, laser heating is predominantly driven by N_2 gas quenching.[40,41] Furthermore, temperature variations indirectly modify the ground-state Larmor frequency by altering the metastable-state density and the MEC rate. Similarly, variations in the RF discharge can change the metastable-state density and thus the MEC-induced frequency shift, while magnetic-field drift directly introduces a Larmor-frequency offset.

However, these effects primarily manifest as static frequency offsets or additional fluctuations; they cannot naturally explain the dispersive detuning dependence observed in the frequency shift. Therefore, the observed behavior is consistent with an MEC-mediated light-shift mechanism, although further experiments are required to characterize these systematic effects in greater detail.

5. Conclusions

MECs are known to affect both the precession frequency and relaxation time of ^{3}He nuclear spins.[18,19] In this work, we show that the pump light can also induce frequency shifts and additional relaxation of ground-state ^{3}He nuclear spins through MECs. We develop a theoretical framework to describe how light-induced effects in the metastable state are transferred to the ground state. In this model, the pump light modifies both the magnetic resonance frequency and linewidth of the metastable state. Owing to the strong coupling between the metastable and ground states mediated by MECs, these light-induced changes lead to an additional frequency shift and enhanced relaxation of the ground-state nuclear spin.

Experimentally, we characterize the light-induced frequency shift and relaxation by comparing FID signals measured with and without the pump light. The results show that the pump light has a pronounced effect at low magnetic fields, while its influence becomes much weaker at higher fields. This result is directly relevant to measurement protocols in which the pump light overlaps the spin-precession interval. In a conventional dark-FID measurement, by contrast, the pump light is extinguished before free precession, so the pump-light-induced shift is absent during the dark interval. We further investigate the dependence of the frequency shift and relaxation on laser detuning and intensity. Since the light-induced frequency shift is tunable through these parameters, it provides an additional degree of freedom for characterizing, reducing, or partially compensating MEC-induced systematic frequency shifts in MEC-based absolute ^{3}He magnetometers. Apart from the frequency-shift and relaxation mechanisms discussed in this paper, minor contributions from changes in atomic number density caused by laser heating and discharge variations, as well as magnetic-field drift, may also contribute to the overall systematic uncertainty and warrant further investigation.

Appendix A: The form of $H_{\rm ls}$

Using the identity

$$(A\cdot B)(C\cdot D)=\sum_{K=0,1,2}(-1)^K(A\otimes C)^K\cdot(B\otimes D)^K, \quad \text{(A1)}$$

where A, B, C, and D are commuting vector operators, the light-shift Hamiltonian $H_{\rm ls}$ can be decomposed into three parts, each expressed as a product of irreducible tensor components. In the hyperfine eigenbasis $|F,m_F\rangle$ of the metastable state, the effective Hamiltonian Eq. (3) can be expressed as follows:

$$\begin{aligned}H_{\rm ls} &= -\frac{I}{2c\varepsilon_0\hbar}Z(\omega;\omega_0)\\ &\quad\times\sum_{K=0,1,2}\sum_{q=-K,\cdots,K}(-1)^{q+K}\{\hat{\varepsilon}^*\otimes\hat{\varepsilon}\}^K_q\alpha^K_{-q}\\ &= -\frac{I}{2c\varepsilon_0\hbar}Z(\omega;\omega_0)\\ &\quad\times\sum_{K=0,1,2}\sum_{q=-K,\cdots,K}\sum_{m_F,m'_F}(-1)^{q+K}\{\hat{\varepsilon}^*\otimes\hat{\varepsilon}\}^K_q\end{aligned}$$

$$\times\langle F_{\rm g}||\alpha^K||F_{\rm g}\rangle\langle F_{\rm g},m_F|F_{\rm g},m'_F;K,-q\rangle|F_{\rm g},m_F\rangle\langle F_{\rm g},m'_F|$$
$$= -\frac{Ie^2}{2c\varepsilon_0\hbar}Z(\omega;\omega_0)\sum_{K=0,1,2}\sum_{q=-K,\cdots,K}(-1)^{q+K}\{\hat{\varepsilon}^*\otimes\hat{\varepsilon}\}^K_q$$
$$\times(-1)^{K+F_{\rm g}+F_{\rm e}}\sqrt{(2F_{\rm g}+1)(2K+1)}\begin{Bmatrix}1 & 1 & K\\ F_{\rm g} & F_{\rm g} & F_{\rm e}\end{Bmatrix}$$
$$\times|\langle F_{\rm g}||\boldsymbol{r}||F_{\rm e}\rangle|^2$$
$$\times\sum_{m_F,m'_F}\langle F_{\rm g},m_F|F_{\rm g},m'_F;K,-q\rangle|F_{\rm g},m_F\rangle\langle F_{\rm g},m'_F|, \quad \text{(A2)}$$

where $f_{ge}=\frac{2m_e\omega_0}{3\hbar}|\langle F_{\rm g}||\boldsymbol{r}||F_{\rm e}\rangle|^2$ is the oscillator strength, $Z(\omega;\omega_0)=1/(\omega_0-\omega-i\gamma_{\rm r}/2)$ is the plasma dispersion function. Note that the coherence between the two hyperfine levels in the metastable is neglected due to the MECs process.[42] Necessary formulas used in the derivation can be found in Ref. [43]. By substituting the specific values of the angular momenta and evaluating the 6-j symbols using Mathematica, we could obtain the reduced Hamiltonian.

The scalar (K=0) part is given by

$$H^{(0)}_{\rm ls} = -\frac{Ie^2}{4m_ec\varepsilon_0}\times\left(f_8\frac{Z(\omega;\omega_8)}{\omega_8}P_{F=1/2}+f_9\frac{Z(\omega;\omega_9)}{\omega_9}P_{F=3/2}\right), \quad \text{(A3)}$$

where $P_{F_i}=\sum_m|F_i,m_{F_i}\rangle\langle F_i,m_{F_i}|$ is the projector operator onto the hyperfine structure.

The vector (K=1) part is given by

$$H^{(1)}_{\rm ls} = \frac{Ie^2}{4m_ec\varepsilon_0}\left(2f_8\frac{Z(\omega;\omega_8)}{\omega_8}\boldsymbol{s}\cdot\boldsymbol{F}_{1/2}+f_9\frac{Z(\omega;\omega_9)}{\omega_9}\boldsymbol{s}\cdot\boldsymbol{F}_{3/2}\right), \quad \text{(A4)}$$

where $\boldsymbol{s}=\frac{(\epsilon^*\times\epsilon)}{i}$ is the mean spin of the photon.

The tensor ($K=2$) part is given by

$$H^{(2)}_{\rm ls} = \frac{Ie^2f_9}{24m_ec\varepsilon_0}\frac{Z(\omega;\omega_9)}{\omega_9}\Big[3(\boldsymbol{\epsilon}\cdot\boldsymbol{F}_{3/2})(\boldsymbol{\epsilon}^*\cdot\boldsymbol{F}_{3/2})+3(\boldsymbol{\epsilon}^*\cdot\boldsymbol{F}_{3/2})(\boldsymbol{\epsilon}\cdot\boldsymbol{F}_{3/2})-2\boldsymbol{F}^2_{3/2}\Big]. \quad \text{(A5)}$$

Appendix B: The Jumper operator $L_{q,F}$

According to the theoretical framework introduced by F. Reiter *et al.* in Ref. [34], for a system consisting of two distinct subspaces — the ground-state subspace and the decaying excited-state subspace — coupled through the interaction $\hat{V}$, with the decay from the excited to the ground subspace described by the jump operators $\hat{L}_k$, the evolution of the whole system can be described by

$$\frac{\rm d}{{\rm d}t}\rho = -{\rm i}[H_{\rm e}+H_{\rm g}+\hat{V},\rho]+\gamma_{\rm r}\sum_k\left(\hat{L}_k\rho\hat{L}^\dagger_k-\frac{1}{2}\{\hat{L}^\dagger_k\hat{L}_k,\rho\}\right), \quad \text{(B1)}$$

where $\gamma_{\rm r}$ is the spontaneous decay rate of the excited states. On the time scale relevant to the ground-state evolution, the fast dynamics of the excited states can be adiabatically eliminated, resulting in an effective equation involving only the ground-state manifold, i.e.

$$\frac{\rm d}{{\rm d}t}\rho_{\rm g} = -{\rm i}[H_{\rm eff},\rho_{\rm g}]+\gamma_{\rm r}\sum_k\left(\hat{L}_{k,\rm eff}\rho_{\rm g}\hat{L}^\dagger_{k,\rm eff}-\frac{1}{2}\{\hat{L}^\dagger_{k,\rm eff}\hat{L}_{k,\rm eff},\rho_{\rm g}\}\right), \quad \text{(B2)}$$

where the effective Hamiltonian and Lindblad operators are given by

$$H_{\rm eff} = -\frac{1}{2}\hat{V}_-[H^{-1}_{\rm NH}+(H^{-1}_{\rm NH})^\dagger]\hat{V}_++H_{\rm g},$$
$$\hat{L}_{k,\rm eff} = \hat{L}_kH^{-1}_{\rm NH}V_+. \quad \text{(B3)}$$

Here, $\hat{V}_-$ and $\hat{V}_+$ denote the de-excitation and excitation parts of $\hat{V}$, respectively, and $H_{\rm NH}=H_{\rm e}-\frac{i}{2}\gamma_{\rm r}\sum_k\hat{L}^\dagger_k\hat{L}_k$ is the non-Hermitian Hamiltonian in the excited-state subspace.

In the ^{3}He system considered here, the excited and ground states correspond to the $|2^3P_0,F=1/2\rangle$ and $|2^3S_1,F=1/2\rangle$ states coupled via the C_8 transition, respectively. The jump operator $\hat{L}_k$ describing the spontaneous decay of the excited state is given by the dimensionless atomic dipole operators $\hat{D}_k$. The interaction Hamiltonian is given by $\hat{V}=\frac{\Omega}{2}\boldsymbol{D}\cdot\hat{\varepsilon}\,{\rm e}^{{\rm i}\omega t}+{\rm h.c.}$, where $\hat{\varepsilon}$ is the polarization vector of the pump light and Ω is the Rabi frequency. By transforming into the rotating frame and applying Eq. (B3), we obtain the effective equation governing the metastable-state dynamics

$$\frac{\rm d}{{\rm d}t}\rho_{\rm m} = -{\rm i}[H_{\rm g}+\delta\hat{\mathcal{E}},\rho_{\rm m}]+\gamma_{\rm r}\sum_\mu\left(L_\mu\rho_{\rm m}L^\dagger_\mu-\frac{1}{2}\{L^\dagger_\mu L_\mu,\rho_{\rm m}\}\right), \quad \text{(B4)}$$

where $\delta\hat{\mathcal{E}}$ is the real part of $H_{\rm ls}$ and the effective jump operators take the form of

$$L_\mu = (-1)^\mu D_{-\mu}\frac{\Omega/2\boldsymbol{D}\cdot\hat{\varepsilon}}{(\omega_0-\omega-{\rm i}\gamma_{\rm r}/2)} = \frac{\Omega/2}{(\omega_0-\omega-{\rm i}\gamma_{\rm r}/2)}\sum_\nu(-1)^{\nu+\mu}\times\sum_K\langle1,-\mu;1,\nu|K,\nu-\mu\rangle T^K_{\nu-\mu}\varepsilon_{-\nu}. \quad \text{(B5)}$$

Specifically, for the left circularly-polarized pump light ($\hat{\varepsilon}=-\hat{e}_+$), the effective jump operators are

$$L_0 = \frac{\Omega/2}{(\omega_0-\omega-{\rm i}\gamma_{\rm r}/2)}\frac{1}{\sqrt{2}}(T^1_1-T^2_1),$$
$$L_1 = \frac{\Omega/2}{(\omega_0-\omega-{\rm i}\gamma_{\rm r}/2)}\left(\frac{1}{\sqrt{3}}T^0_0-\frac{1}{\sqrt{2}}T^1_0+\frac{1}{\sqrt{6}}T^2_0\right),$$

$$L_{-1} = \frac{\Omega/2}{(\omega_0 - \omega - \mathrm{i}\gamma_r/2)} T_2^2, \tag{B6}$$

where $T_q^K(F,F)$ is the irreducible tensor operator. In the numerical simulation, Doppler broadening due to atomic thermal motion must be taken into account, as it modifies the transition rates associated with the jump operators L_μ. The relevant parameters are listed in Table 1.

Acknowledgment

Project supported by the National Natural Science Foundation of China (Grant No. U2230207).

References

[1] Walters G K, Colegrove F D and Schearer L D 1962 *Phys. Rev. Lett.* **8** 439
[2] Anthony P L, Arnold R G, Band H R, *et al.* 1996 *Phys. Rev. D* **54** 6620
[3] Karpuk S, Allmendinger F, Burghoff M, *et al.* 2013 *Phys. Part. Nucl.* **44** 904
[4] Gemmel C, Heil W, Karpuk S, Lenz K, Ludwig C, Sobolev Y, Tullney K, Burghoff M, Kilian W, Knappe-Grüneberg S, Müller W, Schnabel A, Seifert F, Trahms L and Baeßler S 2010 *Eur. Phys. J. D* **57** 303
[5] Walker T and Larsen M 2016 *Advances In Atomic, Molecular, and Optical Physics* vol. 65 (Elsevier) p. 373
[6] Gentile T R, Nacher P J, Saam B and Walker T G 2017 *Rev. Mod. Phys.* **89** 045004
[7] Safronova M S, Budker D, DeMille D, Kimball D F J, Derevianko A and Clark C W 2018 *Rev. Mod. Phys.* **90** 025008
[8] Cong L, Ji W, Fadeev P, Ficek F, Jiang M, Flambaum V V, Guan H, Jackson Kimball D F, Kozlov M G, Stadnik Y V and Budker D 2025 *Rev. Mod. Phys.* **97** 025005
[9] Zhang K Y, Wu L Y and Yan H 2025 *Phys. Rev. Lett.* **135** 131001
[10] Dantan A, Reinaudi G, Sinatra A, Laloë F, Giacobino E and Pinard M 2005 *Phys. Rev. Lett.* **95** 123002
[11] Serafin A, Fadel M, Treutlein P and Sinatra A 2021 *Phys. Rev. Lett.* **127** 013601
[12] Katz O, Reches E, Shaham R, Poem E, Gorshkov A V and Firstenberg O 2025 *Phys. Rev. Res.* **7** 043345
[13] Lu Y, Abdukerim E, Li B, Lei L, Wu T and Guo H 2025 *Phys. Rev. Res.* **7** 043106
[14] Nacher P and Leduc M 1985 *J. Phys.* **46** 2057
[15] Partridge R B and Series G W 1966 *Proc. Phys. Soc.* **88** 983
[16] Zhan Y, Peng X, Li S, Zhang L, Chen J and Guo H 2019 *Opt. Express* **27** 20694
[17] Zhan Y, Peng X, Li S, Zhang L, Chen J and Guo H 2019 *Appl. Phys. B* **125** 170
[18] Dupont-Roc J, Leduc M and Laloë F 1973 *J. Phys.* **34** 961
[19] Dupont-Roc J, Leduc M and Laloë F 1973 *J. Phys.* **34** 977
[20] Colegrove F D, Schearer L D and Walters G K 1963 *Phys. Rev.* **132** 2561
[21] Schearer L D, Colegrove F D and Walters G K 1963 *Rev. Sci. Instrum.* **34** 1363
[22] Dehmelt H G 1964 *Rev. Sci. Instrum.* **35** 768
[23] Schearer L D, Colegrove F D and Walters G K 1964 *Rev. Sci. Instrum.* **35** 767
[24] Wu L Y, Fu C and Yan H 2025 *Meas. Sci. Technol.* **37** 025003
[25] Sato T, Ichikawa Y, Kojima S, *et al.* 2018 *Phys. Lett. A* **382** 588
[26] Xue L, Dong H, Luo W, Ge J and Liu H 2021 *J. Phys.: Conf. Ser.* **1754** 012156
[27] Ingleby S, Griffin P, Dyer T, Mrozowski M and Riis E 2022 *Sci. Rep.* **12** 12888
[28] Li E, Ma Q, Liu G, Yun P and Zhang S 2023 *Phys. Rev. Appl.* **20** 014029
[29] Wu L, Fu C and Yan H 2025 *Chin. Phys. Lett.* **42** 120301
[30] Shifrin V, Park P G, Kim C G, Khorev V and Choi C H 1997 *IEEE Trans. Instrum. Meas.* **46** 97
[31] Mohr P J, Newell D B, Taylor B N and Tiesinga E 2025 *Rev. Mod. Phys.* **97** 025002
[32] Happer W and Mathur B S 1967 *Phys. Rev.* **163** 12
[33] Lee J 2019 *New Constraints on the Axion's Coupling to Nucleons from a Spin Mass Interaction Limiting Experiment (SMILE)* (Ph.D. thesis) (Princeton University)
[34] Reiter F and Sørensen A S 2012 *Phys. Rev. A* **85** 032111
[35] Batz M, Nacher P J and Tastevin G 2011 *J. Phys.: Conf. Ser.* **294** 012002
[36] Dupont-Roc J, Leduc M and Laloë F 1971 *Phys. Rev. Lett.* **27** 467
[37] Batz M 2011 *Metastability Exchange Optical Pumping in ^{3}He Gas up to 30 mT: Efficiency Measurements and Evidence of Laser-Induced Nuclear Relaxation/* (Ph.D. thesis) (Université Pierre et Marie Curie-Paris VI)
[38] Allred J C, Lyman R N, Kornack T W and Romalis M V 2002 *Phys. Rev. Lett.* **89** 130801
[39] Appelt S, Ben-Amar Baranga A, Young A R and Happer W 1999 *Phys. Rev. A* **59** 2078
[40] Lancor B and Walker T G 2010 *Phys. Rev. A* **82** 043417
[41] Wang B, Zhang J, Lu Y, Huang C, Wang T, Qin Z, Dong Y, Zheng Y, Li J, Zhang W, Ye F, Qi X, Liu Y and Tong X 2023 *J. Appl. Phys.* **133** 173105
[42] Courtade E, Marion F, Nacher P J, Tastevin G, Kiersnowski K and Dohnalik T 2002 *Eur. Phys. J. D* **21** 25
[43] Steck D A 2007 *Quantum and Atom Optics*